Jahn-Teller driven electronic instability in thermoelectric tetrahedrite

Article

Accepted Version

Long, S. O., Powell, A., Hull, S., Orlandi, F., Tang, C. C., Supka, A. R., Fornari, M. and Vaqueiro, P. ORCID: https://orcid.org/0000-0001-7545-6262 (2020) Jahn-Teller driven electronic instability in thermoelectric tetrahedrite. Advanced Functional Materials, 30 (12). 1909409. ISSN 1616-3028 doi: 10.1002/adfm.201909409 Available at https://centaur.reading.ac.uk/88295/

It is advisable to refer to the publisher's version if you intend to cite from the work. See Guidance on citing.

www.reading.ac.uk/centaur

CentAUR

Central Archive at the University of Reading

Reading's research outputs online

Jahn-Teller Driven Electronic Instability in Thermoelectric Tetrahedrite

Sebastian O. Long, Anthony V. Powell, Stephen Hull, Fabio Orlandi, Chiu C. Tang, Andrew R. Supka, Marco Fornari, and Paz Vaqueiro*

Sebastian O. Long, Prof Anthony V. Powell
Department of Chemistry, University of Reading, Whiteknights, Reading RG6 6AD, England, United Kingdom

Dr Stephen Hull, Dr Fabio Orlandi
STFC, Rutherford Appleton Laboratory, ISIS Facility, Didcot OX11 0QX, United Kingdom

Dr Chiu C. Tang
Diamond Light Source, Harwell Science and Innovation Campus, Didcot OX11 0DE, United Kingdom

Dr Andrew R. Supka, Prof Marco Fornari
Department of Physics and Science of Advanced Materials Program, Central Michigan University, Mt. Pleasant, Michigan 48859, United States

Dr Paz Vaqueiro
Department of Chemistry, University of Reading, Whiteknights, Reading RG6 6AD, England, United Kingdom
E-mail: p.vaqueiro@reading.ac.uk

Abstract

Tetrahedrite, $Cu_{12}Sb_4S_{13}$, is an abundant mineral with excellent thermoelectric properties owing to its low thermal conductivity. The electronic and structural origin of the intriguing physical properties of tetrahedrite, including its metal-to-semiconductor transition, remains largely unknown. This work presents the first determination of the low-temperature structure of tetrahedrite that accounts for its unique properties. Contrary to prior conjectures, our results show that the trigonal-planar copper cations remain in planar coordination below the metal-to-semiconductor transition. The atomic displacement parameters of the trigonal-planar copper cations, which have been linked to low thermal conductivity, increase by 200% above the metal-to-semiconductor transition. The phase transition is consequence of the orbital degeneracy of the highest occupied $3d$ cluster orbitals of the copper clusters found inside the sodalite cages in the cubic phase. This study reveals that a Jahn-Teller electronic instability leads to the formation of "molecular-like" Cu_5^{7+} clusters and suppresses copper rattling vibrations due to the strengthening of direct copper-copper interactions. Our first-principles calculations demonstrate that the structural phase transition opens a small band gap in the electronic density of states and eliminates the unstable phonon modes. The present results provide insights on the interplay between phonon transport, electronic properties and crystal structure in mixed-valence compounds.

1. Introduction

Tetrahedrite, $Cu_{12}Sb_4S_{13}$, which is a mixed-valence compound, $(Cu^{2+})_2(Cu^+)_{10}(Sb^{3+})_4(S^{2-})_{13,}$ is highly attractive as a sustainable and environmentally-friendly *p*-type thermoelectric material.[1] Its ultralow and glass-like thermal conductivity is critically important for efficient thermal-to-electrical (thermoelectric) energy conversion, while its mixed-valence character provides a fascinating playground to investigate the interplay between phonon transport, electronic properties and potential charge ordering effects. Tetrahedrite, which is also attracting attention as a potential photovoltaic material,[2] crystallises in a collapsed sodalite structure (**Figure 1**),[3] in which corner-sharing CuS_4 tetrahedra form truncated octahedral cages. Inside each cage, there is a sulfur anion octahedrally coordinated to six trigonal-planar copper cations (Figure 1(b)). The ultralow thermal conductivity of tetrahedrite has been linked to rattling vibrations of the trigonal-planar copper cations (Figure 1(c)). [4]

Despite its importance, the understanding of the electronic origin of the anharmonic behaviour of the trigonal-planar copper cations in tetrahedrite and of the phonon modes involved is still limited: phonon calculations for the cubic structure of tetrahedrite lead to unstable optical phonon branches,[1(b)] indicating that $Cu_{12}Sb_4S_{13}$ undergoes a structural transition at low temperatures. Therefore elucidation of the low-temperature structure is critical in order to understand the complex lattice dynamics of tetrahedrite. However, previous low-temperature studies are contradictory and inconclusive.[5] The structural transition in tetrahedrite is accompanied by a metal-to-semiconductor transition (MST).[6] In mixed-valence transition-metal compounds, a MST is often associated with charge ordering, and either a nonmagnetic (e.g. $CuIr_2S_4$)[7] or a magnetically-ordered ground state (e.g. Fe_3O_4).[8] Orbital ordering, as exemplified by that found below the Verwey transition for the 3-atom linear trimerons in Fe_3O_4,[8] can also occur. The nature of the magnetic ground state of tetrahedrite,[9] and the origin of the MST have so far proven elusive. Here, we report the determination of the crystal structure of tetrahedrite below the MST. We demonstrate that this structural transition is associated with a unique Jahn-Teller distortion of the octahedral Cu_6^{7+}

clusters found inside the sodalite cages. Our experimental and computational results demonstrate that the structural transition, which suppresses the copper rattling vibrations due to a strengthening of intra-cluster copper-copper interactions, is coupled to a MST, which opens a band gap at the top of the valence band. The two holes per formula unit present in $Cu_{12}Sb_4S_{13}$, which are delocalised above the MST, become localised within "molecular-like" pentameric Cu_5^{7+} clusters below the phase transition.

2. Results and Discussion

Powder neutron diffraction data collected on tetrahedrite reveal that additional reflections emerge on cooling below 90 K (**Figure 2**), which cannot be indexed on the basis of the original cubic unit cell (a_c). However, these peaks can be indexed on the basis of a tetragonal supercell, with lattice parameters $a_t = \sqrt{2} \ a_c$, $c_t = a_c$. Significantly, subtraction of neutron diffraction data at long d-spacing collected at 80 K, just below the phase transition, from those collected at 1.5 K does not lead to any residual intensity, demonstrating that there is no magnetic scattering at low temperatures and hence no long-range magnetic order. High-resolution synchrotron X-ray data collected below 90 K also contain additional reflections, indexable on the same tetragonal supercell (Figure 2). A symmetry analysis using ISODISTORT[10] produced five possible distorted structures, described in subgroups of the parent cubic phase ($I\bar{4}3m$): $P\bar{4}$, $P\bar{4}m2$, $P\bar{4}c2$, $P\bar{4}b2$ and $P\bar{4}n2$. Each of these structural configurations was utilized as a starting model for Rietveld refinements using neutron diffraction data collected below the phase transition. The data were best described in the space group $P\bar{4}c2$, which was subsequently used in all structural refinements below the MST. The alternative space groups, as well as those using a larger $2a_c \times 2a_c \times 2a_c$ supercell, resulted in unstable refinements, significantly higher residuals and/or physically meaningless atomic displacement parameters. Representative observed and calculated profiles for Rietveld refinements for the cubic ($I\bar{4}3m$) and tetragonal ($P\bar{4}c2$) phases are presented in Figure 2 and the Supplementary Information. ISODISTORT indicates that the primary order parameter for the phase transition is (a, a, 0,0,0,0), belonging to the irreducible representation N_3, at the k-point [½, ½, 0] of the cubic unit cell. First-

principles total-energy calculations for tetrahedrite, as the cubic structure becomes increasingly distorted, indicate that the phase transition to the tetragonal phase results in a small stabilisation of the structure, by -0.06 Ry (Supplementary Information). At the phase transition, the lattice parameters diverge sharply (Figure 2(d)), and then show little variation ($< 0.2\%$) on further cooling. The marked discontinuity in the unit-cell volume at the phase transition, together with the coexistence of the cubic and tetragonal phases visible on X-ray diffraction data collected at 80 K, indicates that the structural phase transition is first order in nature.

The phase transition involves large displacements of the octahedrally-coordinated sulfur atom, S(2), at the center of the sodalite cage and of the copper atom in trigonal coordination, Cu(2), with respect to their undistorted positions in the cubic unit cell (Figure 1). In the cubic phase, S(2) is located at the centre of an ideal octahedron, with six identical Cu-S distances and Cu-S-Cu bond angles of 90° (**Figure 3**(a)). The transition to a tetragonal structure results in a marked displacement of the octahedral S(2), corresponding to a shift from the position at the centre of the sodalite cage towards the square windows of the sodalite cage (Figure 3(b)). At the same time, the distances to the two copper cations in "axial" positions change substantially at the phase transition, one expanding by *ca*. 9% to 2.45 Å and the other contracting by ca. 6% to 2.12 Å.

These variations in bond distances are accompanied by significant angular distortions of the $S(2)Cu(2)_6$ octahedron (Supplementary Information). The changes in bonding are illustrated by the difference between the electron localisation functions (ELF) of the cubic and tetragonal structures (Figure 3(c)). The displacement of the S(2) anion propagates, in an alternating fashion, along the [110] and [$\bar{1}$10] directions of the tetragonal unit cell (Figure 3(d)). The structural distortion of coordination polyhedra can be quantified using the bond angle variance, σ^2,[11] along with the bond length deviation, Δ,[12] with large values of the distortion parameters expected for polyhedra containing Jahn-Teller ions.[13] Whilst values of σ^2 and Δ for the $Cu(1)S_4$ tetrahedra are small and change very little at the phase transition (Supplementary Information), we find values of σ^2 as high as 647 for the $S(2)Cu(2)_6$ octahedron and the trigonal-planar $Cu(2)S_3$ units, indicating that large

5

polyhedral distortions occur as a result of the structural phase transition. The large polyhedral distortion observed for the S(2)Cu(2)$_6$ octahedron is accompanied by remarkable shortening and lengthening of Cu(2)-Cu(2) distances, by approximately 0.4 Å (Figure 3(e), 3(f) and 3(g)), with short copper-copper interactions resulting in the formation of copper pentameric clusters (Figure 3(g)). While at room temperature all Cu(2)-Cu(2) distances are 3.179(1) Å, short distances of 2.673(3), 2.857(4) and 2.957(3) Å are found at 1.5 K. These short Cu(2)-Cu(2) distances are close to or below the sum of the van der Waals radii (2.8 Å) of two copper atoms, and compare to those found in copper metal (2.556 Å),[14] or in copper(II) acetate dimers (2.64 Å).[15] Cuprophilic d^{10}-d^{10} interactions in copper(I) compounds, reflected in short copper-copper distances between 2.34 and 2.79 Å, are known to influence the structure of these compounds, which often contain cluster-like assemblies of d^{10} cations.[16] Short copper-copper distances are also found in compounds containing copper(II), of which copper(II) acetate dimers are perhaps the most studied example.[17] In copper(II) dimers, coupling of the unpaired electron on each copper(II) centre through weak metal-metal interactions may lead to antiferromagnetic or ferromagnetic interactions, depending on whether the ground state is a spin singlet (electrons paired) or a spin triplet (parallel electrons).[18] In order to unravel the origin of the structural transition in tetrahedrite, we carried out a molecular orbital analysis of the metal cluster formed by the trigonal-planar copper cations above and below the phase transition (Figure 3(f) and 3(g)). Taking into account that tetrahedrite is a mixed-valence compound, and that in the cubic phase the Cu^{2+} cations are delocalised, the average copper oxidation state is +1.167, and the octahedral cluster is therefore formulated Cu_6^{7+}. Our extended Hückel calculations for a bare Cu_6^{7+} cluster (point group O_h), which agree with previous work on octahedral molecular clusters,[19] indicate that the highest occupied molecular orbital (HOMO), containing 5 electrons, is t_{1g}. This results in a degenerate electronic state, $^2T_{1g}$, able to undergo a Jahn-Teller distortion. Below the phase transition, ^{63}Cu NMR indicates that there is no internal magnetic field at the tetrahedral Cu(1) site, and since Cu(1) is non-magnetic in the tetragonal phase,[9(b)],[20] the Cu^{2+} cations must be located in trigonal-planar sites. The low distortion

6

parameters for the Cu(1)S$_4$ tetrahedra are not consistent with the presence of d^9 Cu^{2+} cations on this site either, while the distortion parameters for the Cu(2)S$_3$ polyhedra, and particularly those in the pentamer, are much higher. We therefore conclude that the pentameric copper cluster should be described as Cu$_5^{7+}$, containing two Cu^{2+} and three Cu$^+$ delocalised within the cluster. Extended Hückel calculations for a distorted square-pyramidal Cu$_5^{7+}$ pentameric cluster (point group C_{2v}) indicate that the ground state is a spin-singlet, diamagnetic state (S = 0), $^1B_1$. Above the phase transition, tetrahedrite may be formulated as $[Cu_6^{+1.167}S]^{5+}[Cu_6^{+1.167}Sb_4S_{12}]^{5-}$, in order to highlight the cluster inside the sodalite cage. The phase transition involves transfer of one electron from the metal cluster inside the sodalite cage to the framework, which may be expressed by formulating tetrahedrite as $[(Cu_5^{+1.4}S)Cu^+]^{6+}[Cu_6^+Sb_4S_{12}]^{6-}$ below the MST. This shows that instead of full charge ordering of Cu^{2+} cations, the two holes per formula unit are spread over the five copper cations in the pentamer.

The magnetic susceptibility, heat capacity and electrical resistivity show clear anomalies at the temperature of the structural phase transition (**Figure 4**). The anomaly at *ca.* 90 K in the temperature dependence of the magnetic susceptibility (Figure 4(a)) can be interpreted as arising from a transition from a paramagnetic state to a nonmagnetic ground state. In the paramagnetic region, a Curie-Weiss fit to the reciprocal Zero-Field-Cooled (ZFC) susceptibility data yields a Weiss constant of -140 K and a Curie constant of 0.48 cm^3 K^{-1} mol^{-1}. This corresponds to an effective magnetic moment, μ_{eff} = 1.5 per Cu^{2+}, consistent with the value expected for spin-only behaviour for a single unpaired electron. Magnetization data collected at 1.5 K show a linear dependence on field, indicating the absence of any spontaneous magnetization at low temperatures (Supplementary Information). This, together with the absence of magnetic scattering in our low-temperature neutron diffraction data and existing ^{63}Cu NMR studies on tetrahedrite, which point to a nonmagnetic ground state[9(b)],[20] is consistent with the creation of a spin-singlet diamagnetic ground state arising from the formation of pentameric Cu$_5^{7+}$ clusters established by our structural analysis. The increase in magnetic susceptibility at low temperatures is likely to be associated with

The marked anomaly in the electrical resistivity at the phase transition temperature (Figure 4(c)) corresponds to the MST. Above the phase transition, electronic band structure calculations show that cubic $Cu_{12}Sb_4S_{13}$ is a metal, with the Fermi level located near the top of the valence band (2 holes per formula unit).[1(b)] Our electronic band structure calculations (Figure 4(d)) reveal that the cubic-to-tetragonal phase transition opens a small gap of *ca.* 0.064 eV at the top of the valence band, and hence results in a marked reduction in the density of states at the Fermi level, as previously inferred from ^{63}Cu NMR measurements.[21] The main contributors to states above the gap are those from S and the Cu_5^{7+} cluster, as shown in Figure 4(e). This is consistent with the semiconducting behaviour observed below 90 K, where the electrical resistivity increases exponentially with decreasing temperature, increasing by a factor of 10^2 from 0.04 mΩm at 90 K to 4 mΩm at 1.5 K. In the low-temperature region ($T < 20$ K), the electrical resistivity shows a $\ln(\rho)$ vs. $T^{1/4}$ dependence, which corresponds to a three-dimensional variable-range-hopping conduction mechanism. This would indicate that the holes are localised in the Cu_5^{7+} clusters, and that conduction occurs by hopping between clusters. As previously reported, $\rho(T)$ shows a second anomaly at *ca.* 200 K, the origin of which has not been established.[5(b)] Our data do not provide any evidence of a structural phase transition coincident with this second anomaly.

The magnitude of the atomic displacement parameter (ADP) of the trigonal-planar Cu cation increases by 200 % at the phase transition, while the ADPs of the other atoms show only a small discontinuity (**Figure 5**(a)). The large and highly anisotropic ADP of the trigonal-planar copper cation in the cubic phase is attributed to rattling vibrations. Two alternative mechanisms have been proposed: it has been suggested that weak bonding interactions of Cu(2) with the lone pairs of two neighbouring antimony cations drive the anharmonic rattling,[4(a)] or that chemical pressure squeezes the Cu(2) cation out of planar coordination, with the amplitude of the out-of-plane rattling increasing when the S_3 triangle is compressed.[4(d)] Contrary to previous work that inferred that the Cu(2) cations are displaced from the S_3 trigonal plane below the MST,[4],[21] our results provide conclusive evidence that the Cu(2) cations remain within the S_3 trigonal plane, but shortening and

8

lengthening of Cu(2)-S distances occurs (Figure 5(b) and Supplementary Information). Moreover, while above the MST the distance between trigonal-planar Cu(2) and each of the two antimony cations is *ca.* 3.38 Å (Figure 5(c)), in the tetragonal phase, there are two short Cu(2)-Sb[(i)] and one long Cu(2)-Sb[(i)] distances of ~ 3.3 and 3.5 Å, and two long Cu(2)-Sb[(ii)] and one short Cu(2)-Sb[(ii)] distances of ~ 3.5 and 3.3 Å. In the ELF map for the tetragonal phase, a "crescent-moon" shape provides evidence of the antimony lone pair, which points towards three Cu(2) cations (Figure 5(e)). However, the most significant change in the coordination environment of the Cu(2) cations is the strengthening of Cu(2)-Cu(2) interactions. This is evidenced by bond valence sum calculations, which show that when metal-metal interactions are considered, below the MST copper-copper interactions contribute to between 10 and 15% of the total bond valence sum. By contrast, in the cubic phase, the contribution of copper-copper interactions is only ~ 5%. We therefore conclude that below the phase transition rattling is suppressed because the Cu(2) cations in the pentamer are "locked" in place due to the strengthening of copper-copper interactions. This is consistent with the disappearance below the MST of the low-energy vibrational mode (*ca.* 3 meV) attributed to the Cu(2) rattling vibration, observed by inelastic neutron scattering.[5(a)] First-principles calculations of the phonon spectrum for the tetragonal phase rule out additional zone-center instabilities (Figure 5(e)), hence confirming its stability. This is in sharp contrast with the phonon spectrum for the cubic phase, in which the main contributors to the unstable phonons are the trigonal-planar Cu(2) cations and the octahedral S(2) anion (Figure 5(f)), both of which undergo large displacements at the phase transition. This indicates that the phonon mode(s) associated with the phase transition involve vibrations of Cu(2) and S(2) atoms.

3. Conclusions

In summary, we have shown that direct copper-copper interactions within the Cu_6^{7+} clusters located inside the sodalite cages are key to understand the remarkable behaviour of tetrahedrite, and in particular the origin of the MST and of its low thermal conductivity. The lattice instability in tetrahedrite is coupled with a Jahn-Teller driven electronic transition and a concomitant magnetic

transition. The cubic-to-tetragonal phase transition involves transfer of one electron from the metal cluster inside the sodalite cage to the framework, and therefore below the MST, the two holes per formula unit are localised within a "molecular-like" pentameric Cu_5^{7+} cluster. These pentamers can be considered a unique example of a large "orbital molecule",[22] where electron delocalisation occurs within the metal cluster, with electronic conduction involving hopping between clusters. While there are numerous examples of dimeric "orbital molecules", larger species, containing more than three atoms, are very rare.[22] Below the phase transition, the strengthening of copper-copper interactions within the pentameric Cu_5^{7+} cluster "locks" the trigonal-planar cations in place, suppressing the out-of-plane rattling vibration to which low thermal conductivity in cubic tetrahedrite has been attributed. Given that a study of the local structure of magnetite has shown that disordered "orbital molecules" persist well above the Verwey transition,[23] disordered pentamers might be present in tetrahedrite above the MST, "hidden" in the average long-range cubic structure, and affect the phonon transport.

The results presented here offer new insights for the search and design of high-performance thermoelectric materials. We envisage that low thermal conductivity may be achieved by engineering Jahn-Teller driven instabilities through mixed valency in materials containing transition metals. Given the major role of direct copper-copper interactions in tetrahedrite, the potential of other materials containing cluster-like assemblies of coinage metal cations for thermoelectric applications should also be explored.

4. Experimental Section

$Cu_{12}Sb_4S_{13}$ was synthesised from a stoichiometric mixture of elemental copper (99.5%, Sigma-Aldrich), antimony (99.5%, Alfa Aesar) and dried sulfur (flakes, 99.99%, Sigma-Aldrich). The elements were initially ground together in an agate mortar. The powdered mixture, together with 6mm stainless-steel milling balls (2:7 mass ratio of powder to balls), was placed in a 25 mL stainless steel milling jar under an argon atmosphere. The sample was milled for 8 h in a Retsch Planetary Ball Mill PM100 operating at 600 rpm, with a change in rotational direction every 30

min. The product was loaded into a tungsten carbide mould and sandwiched between graphite foil and tungsten carbide plungers. The mould was heated to 693 K under a nitrogen atmosphere and a pressure of 125 MPa was applied for 30 minutes both to complete synthesis and consolidate the sample. The pelletized sample was then ground into a powder using an agate mortar, for the collection of diffraction and magnetic susceptibility data. A portion of the powdered sample was hot-pressed for a second time, under the same conditions and a density greater than 98% of the theoretical density achieved, to provide consolidated disks for electrical transport and thermal property measurements. All tetrahedrite samples with composition $Cu_{12}Sb_4S_{13}$ contain small amounts of Cu_3SbS_4, in agreement with previous literature reports.[1] In addition, the sample used for the neutron experiment contains a small amount of a copper-rich tetrahedrite, $Cu_{12+x}Sb_4S_{13}$,[4(c)] which remains cubic at all temperatures.

For initial sample characterisation, powder X-Ray diffraction data were collected using a Bruker D8 Advance (Cu Kα$_1$: λ = 1.5405 Å) diffractometer, equipped with a LynxEye detector and a Ge monochromator. Powder neutron diffraction data were collected using the WISH diffractometer at the ISIS Facility. The powdered sample was loaded into a thin-walled vanadium can that was placed in a cryostat. Data were collected on cooling over the range 120 ≥ T/K ≥ 1.5 and on subsequent heating to 300K in temperature steps of 10 – 20K, depending on temperature. Synchrotron X-ray data were collected using the beamline I11 (high resolution powder diffraction)[24] at the Diamond Light Source (UK), using high-resolution MAC detectors and a calibrated wavelength of 0.824513(10) Å. The sample powder was coated on the surface of an aluminium wire attached to a copper holder, using a small amount of hand cream. The sample and holder were attached to a PheniX cryostat, which was used to collect data on heating between 10 K and 300 K. Rietveld refinements were carried out using the GSAS software.[25] In the refinements using WISH data,[26] three detector banks were included (average 2θ = 90°, 120° and 150°). The atomic displacement parameter (ADP) of the trigonally coordinated copper cation, Cu(2), in the high-temperature cubic phase, was modelled anisotropically, whereas an isotropic value was used for the low-temperature

11

phase. The ADPs of all sulfur sites were constrained to be equal at a given temperature. A similar constraint was applied for the tetrahedral copper sites, trigonal planar copper sites and antimony sites in the low temperature phase. The resulting crystallographic parameters are presented as Supplementary Information. Rietveld refinements indicate that the sample used for the neutron experiment contains 84.39(3) wt% of a tetrahedrite phase with a =10.3289(2) Å, 7.70(7) wt% of the second tetrahedrite phase with an enlarged unit cell and 7.92(4) wt% of Cu_3SbS_4. Rietveld refinement using synchrotron data collected at room temperature on a second sample prepared under similar conditions, indicate that this sample contains 92.29(2) wt% of a tetrahedrite phase with a = 10.33245(3) Å and 7.71(6) wt% of Cu_3SbS_4. The values of bond angle variance, σ^2, and bond length deviation, Δ, were determined using:

$$\sigma_{poly}{}^2 = \frac{1}{m-1}\sum_{i=1}^{m}(\theta_i - \theta_{poly})^2 \quad (1)$$

$$\Delta_n = \frac{1}{n}\sum_{i=1}^{n}[(l_i - \bar{l})/\bar{l}]^2 \times 1000 \quad (2)$$

where the subscript 'poly' refers to the type of polyhedron (octahedron, tetrahedron or trigonal planar), with angles, θ_{poly}, (90°, 109.47° and 120° respectively) and the summation is taken over the m angles of the polyhedron or the n vertexes of the polyhedron, while l_i and $\bar{l}$ are the individual and mean copper-sulfur distances respectively. Metal-metal bond valence sums were calculated following the approach described by O'Keeffe.[27] Extended Hückel calculations, to determine qualitative molecular orbital diagrams for copper clusters, were carried out using Hyperchem. Magnetic susceptibility data were collected using a Quantum Design MPMS XL-7 SQUID Magnetometer. Data were collected over the temperature range $1.5 \leq T/K \leq 300$ both after cooling in zero applied field (ZFC) and after cooling in the measuring field (FC) of 10 kG. Magnetization data were also collected at 1.5 K as a function of field over the field range $-10000 \leq H/G \leq 10000$. Corrections were applied to the data to account for the diamagnetic contribution from each element and the contribution from the gelatin capsule.

Electrical resistivity and heat capacity data were collected on a Quantum Design PPMS-9 Physical Property Measurement System. The electrical resistivity was measured using the Van der Pauw

method with electrical contacts at corners of the face of an 8×8 mm square pellet. Data were collected over the temperature range $1.5 \le T/\,K \le 300$, while the specific heat, measured on a fragment of the same pellet, was measured over the temperature range $1.5 \le T/\,K \le 300$. First-principles calculations of band structures, density of states, and phonon modes were computed using the Quantum Expresso package[28] as integrated in AFLOWπ.[29] We used ultrasoft PBE pseudopotentials,[30] well converged basis sets corresponding to an energy cut-off of 60 Ry for the wavefunctions and 480 Ry for the charge density. Local Hubbard U corrections were 1.09 eV for S, 0.01 eV for Sb, 8 eV for Cu(1) and 6 eV for Cu(2).

To integrate over the Brillouin zone, we used a 4 x 4 x 6 grid. Figure 4(e) has been obtained by interpolating between the cubic structure and the low temperature tetragonal ground state. Phonons were computed with the finite difference method as implemented in AFLOWπ.[29] The lattice parameters agree with experimental values within 2%.

Supporting Information

Neutron Rietveld profiles for all WISH banks at 1.5 K, temperature dependence of lattice parameters, bond distances and angles for Cu(2), energy calculations as a function of cubic-to-tetrahedral distortion, molecular orbital diagrams for copper clusters, structural diagrams, magnetic field sweep and tabulated crystallographic information Rietveld refinements using WISH and I11 diffraction data and distortion parameters.

Conflict of interest
The authors declare no conflict of interest

References

[1] a) R. Chetty, A. Bali, R.C. Mallik, *J. Mater. Chem. C* **2015** *3*, 12364; b) X. Lu, D. T. Morelli, Y. Xia, F. Zhou, V. Ozolins, H. Chi, X. Zhou, C. Uher *Adv. Energy Mater.* **2013**, *3*, 342; c) M.K. Jana, K. Biswas, *ACS Energy Lett.* **2018**, *3*, 1315.

[2] a) J. Heo, R. Ravichandran, C. F. Reidy, J. Tate, J. F. Wager, D. A. Keszler, *Adv. Energy Mater.* **2015,** *5*, 1401506; b) M. Tamilselvan, A. J. Bhattacharyya, *ACS Appl. Energy Mater.* **2018**, *1*, 4227.

[3] a) B. J. Wuensch, *Z. Kristallogr.* **1964**, *119*, 437; b) N.E. Johnson, J. R. Craig, J. D. Rimstidt, *Am. Mineral.* **1988**, *73*, 389.

[4] a) K. Suekuni, K. Tsuruta, M. Kunii, H. Nishiate, E. Nishibori, S. Maki, M. Ohta, A. Yamamoto, M. Koyano, *J. Appl. Phys.* **2013**, *113*, 043712; b) W. Lai, Y. Wang, D.T. Morelli, X. Lu, *Adv. Funct. Mater.* **2015**, *25*, 3648; c) Y. Bouyrie, C. Candolfi, S. Pailhès, M.M. Koza, B. Malaman, A. Dauscher, J. Tobola, O. Boisron, L. Saviot, B. Lenoir, *Phys. Chem. Chem. Phys.* **2015**, *17*, 19751; d) P. Vaqueiro, G. Guélou, A. Kaltzoglou, R.I. Smith, T. Barbier, E. Guilmeau, A.V. Powell, *Chem. Mater.* **2017**, *29*, 4080; e) K. Suekuni, C. H. Lee, H. I. Tanaka, E. Nishibori, A. Nakamura, H. Kasai, H. Mori, H. Usui, M. Ochi, T. Hasegawa, M. Nakamura, S. Ohira-Kawamura, T. Kikuchi, K. Kaneko, H. Nishiate, K. Hashikuni, Y. Kosaka, K. Kuroki, T. Takanatake, *Adv. Mater.* **2018**, *30*, 1706230.

[5] a) A. F. May, O. Delaire, J. L. Niedziela, E. Lara-Curzio, M. A. Susner, D. L. Abernathy, M. Kirkham, M. A. McGuire, *Phys. Rev. B* **2016**, *93*, 064104; b) H. I. Tanaka, K. Suekuni, K. Umeo, T. Nagasaki, H. Sato, *J. Phys. Soc. Japan* **2016**, *85*, 014703; c) V. R. Hathwar, A. Nakamura, H. Kasai, K. Suekuni, H. I. Tanaka, T. Takabatake, B. B. Iversen, E. Nishibori, *Cryst. Growth Des.* **2019**, *19*, 3979-3988.

[6] K. Suekuni, K. Tsuruta, T. Ariga, M. Koyano, *Appl. Phys. Express* **2012**, *5*, 051201.

[7] P. G. Radaelli, Y. Horibe, M.J. Gutmann, H. Ishibashi, C. H. Chen, R. M. Ibberson, Y. Koyama, Y. S. Hor, V. Kiryukhin, S. W. Cheong, *Nature* **2002**, *416*, 155.

[8] M. S. Senn, J. P. Wright, J. P. Attfield, *Nature* **2012**, *481*, 173.

[9] a) F. Di Benedetto, G. P. Bernardini, C. Cipriani, C. Emiliani, D. Gatteschi, M. Romanelli, *Phys. Chem. Minerals* **2005**, *32*, 155; b) S. Kitagawa, T. Sekiya, S. Araki, T. C. Kobayashi, K. Ishida, T. Kambe, T. Kimura, N. Nishimoto, K. Kudo, M. Nohara, *J. Phys. Soc. Japan* **2015**, *84*, 093701.

[10] B. J. Campbell, H. T. Stokes, D. E. Tanner, D. M. Hatch, *J. Appl. Cryst*. **2006**, *39*, 607.

[11] K. Robinson, G. V. Gibbs, P. H. Ribbe, *Science* **1971**, *172*, 567.

[12] R. D. Shannon, *Acta Cryst. A* **1976**, *32*, 751.

[13] M. E. Fleet, *Mineral. Mag*. **1976**, *40*, 531.

[14] E. A. Owen, E. L. Yates, *Philos. Mag.* **1933**, *15*, 472.

[15] R. L. Carlin. *Magnetochemistry*, Springer-Verlag, Berlin, **1986**, Chapter 5.

[16] M. Jansen, *Angew Chem. Int. Ed. Engl.* **1987**, *26*, 1098.

[17] a) J. Catterick, P. Thornton, *Adv. Inorg. Chem. Radiochem.* **1977**, *20*, 291; b) M. Kato, Y. Muto, *Coord. Chem. Rev.* **1988**, *92*, 45.

[18] O. Kahn, *Angew. Chem. Int. Ed. Engl.* **1985**, *24* 834.

[19] R. G. Wooley, *Inorg. Chem.* **1985**, *24*, 3519.

[20] N. Ghassemi, X. Lu, Y. Tian, E. Conant, Y. Yan, X. Zhou, J. H. Ross, *ACS Appl. Mater. Interfaces*, **2018**, *10*, 36010.

[21] T. Matsui, H. Matsuno, H. Kotegawa, H. Tou, K. Suekuni, T. Hasegawa, H. I. Tanaka, T. Takabatake, *J. Phys. Soc. Japan* **2019**, *88*, 054710.

[22] J. P. Attfield, APL *Materials* **2015**, *3*, 041510.

[23] G. Perversi, E. Pachoud, J. Cumby, J. M. Hudspeth, J. P. Wright, S. A. J. Kimber, J. P. Attfield, *Nat. Commun.* **2019**, *10*, 2857.

[24] S. P. Thompson, J. E. Parker, J. Potter, T. P. Hill, A. Birt, T. M. Cobb, F. Yuan, C. C. Tang, *Rev. Sci. Instrum.* **2009**, *80*, 075107.

[25] A. C. Larson, R. B. Von Dreele, General Structure Analysis System. Los Alamos National Laboratory Report LAUR **1994**, 86−784.

[26] P. Vaqueiro, S.O. Long, A.V. Powell, F. Orlandi, STFC ISIS Neutron and Muon Source, **2016** https://doi.org/10.5286/ISIS.E.RB1620283

[27] M. O'Keeffe, N. E. Brese, *J. Am. Chem. Soc.* **1991**, *113*, 3226.

[28] a) P. Giannozzi, S. Baroni, N. Bonini, M. Calandra, R. Car, C. Cavazzoni, D. Ceresoli, G. L Chiarotti, M. Cococcioni, I. Dabo, A. Dal Corso, S. de Gironcoli, S. Fabris, G. Fratesi, R. Gebauer, U. Gerstmann, C. Gougoussis, A. Kokalj, M. Lazzeri, L. Martin-Samos, N. Marzari, F. Mauri, R. Mazzarello, S. Paolini, A. Pasquarello, L. Paulatto, C. Sbraccia, S. Scandolo, G. Sclauzero, A. P. Seitsonen, A. Smogunov, P. Umari R. M. Wentzcovitch, *J. Phys.: Condens. Matter* **2009**, *21*, 395502; b) P. Giannozzi, O. Andreussi, T. Brumme, O. Bunau, M. B. Nardelli, M. Calandra, R. Car, C. Cavazzoni, D. Ceresoli, M. Cococcioni, N. Colonna, I. Carnimeo, A. Dal Corso, S. de Gironcoli, P. Delugas, R. A. DiStasio Jr, A. Ferretti, A. Floris, G. Fratesi, G. Fugallo, R. Gebauer, U. Gerstmann, F. Giustino, T. Gorni, J. Jia, M. Kawamura, H-Y. Ko, A. Kokalj, E. Küçükbenli, M. Lazzeri, M. Marsili, N. Marzari, F. Mauri, N. L. Nguyen, H-V. Nguyen, A. Otero-de-la-Roza, L. Paulatto, S. Poncé, D. Rocca, R. Sabatini, B. Santra, M. Schlipf, A. P. Seitsonen, A. Smogunov, I. Timrov, T. Thonhauser, P. Umari, N. Vast, X. Wu, S. Baroni. *J. Phys.: Condens. Matter* **2017**, *29*, 465901.

[29] A. R. Supka, T. E. Lyons, L. Liyanage, P. D'Amico, R. Al Rahal Al Orabi, S. Mahatara, P. Gopal, C. Toher, D. Ceresoli, A. Calzolari, S. Curtarolo, M. B. Nardelli, M. Fornari, *Comput. Mater. Sci.* **2017**, *136*, 76.

[30] a) D. R. Hamann, *Phys. Rev. B* **2013**, *88*, 085117; b) G. Prandini, A. Marrazzo, I. E. Castelli, N. Mounet, N. Marzari,. *Npj Comput. Mater.* **2018**, *4*, 72.
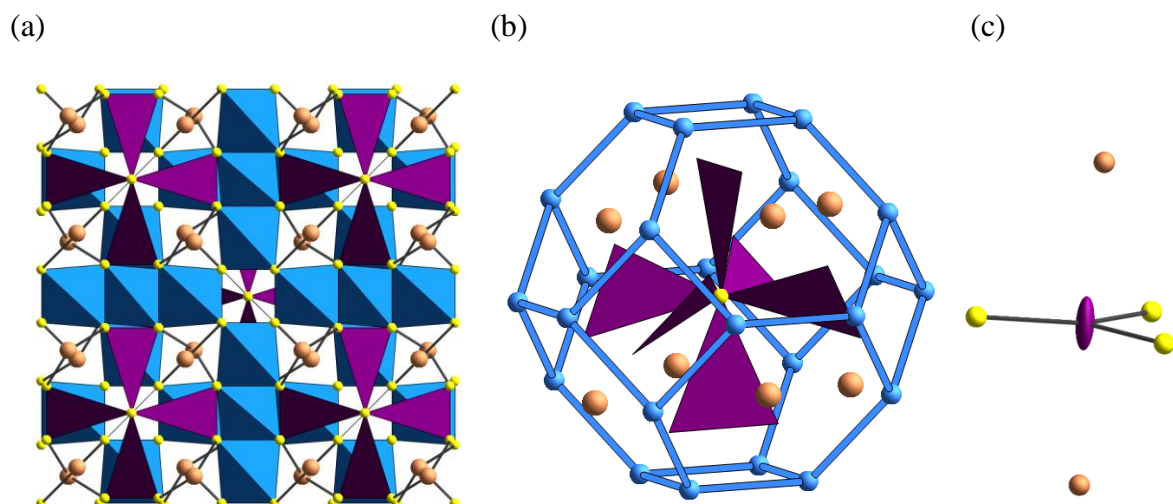
(a)   (b)   (c)

Figure 1. – (a) View of the crystal structure of tetrahedrite along the *c*-axis. Key: Blue – Cu(1)S$_4$ tetrahedra ; purple – Cu(2)S$_3$ trigonal planar unit; orange – antimony atoms; yellow – sulfur atoms. (b) A truncated octahedral sodalite cage, with each CuS$_4$ shown as a node; the sulfur atom at the center is denoted S(2) in the text. (c) Coordination of the trigonal planar copper cation, Cu(2), showing its highly anisotropic atomic displacement parameter
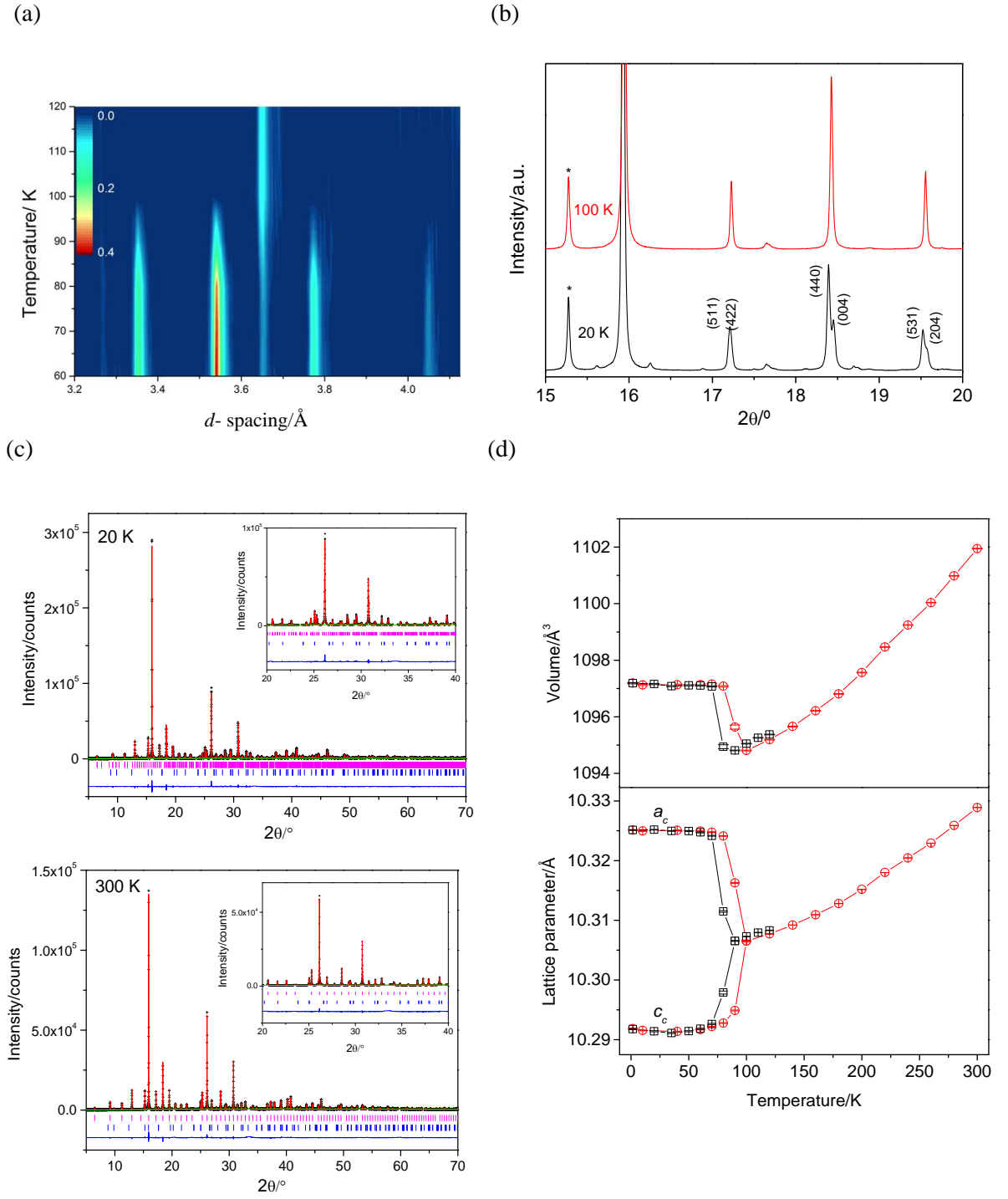
Figure 2. – (a) Powder neutron diffraction data as a function of temperature, over a selected range of d-spacings, showing the appearance of additional reflections; (b) selected synchrotron diffraction data (λ=0.82451 Å), collected below and above the transition, showing the splitting of existing reflections and the appearance of new reflections. Peak from the impurity phase, Cu_3SbS_4, has been labelled with a star. (c) Rietveld refinements using synchrotron X-ray diffraction data collected on $Cu_{12}Sb_4S_{13}$ at 300 and 20 K. Observed, calculated and difference profiles are denoted by black points, a red solid line and a blue line, respectively. The pink and blue reflection markers are for the tetrahedrite phase and the Cu_3SbS_4 impurity, respectively. Insets have been added to illustrate the difference between 300 K and low-temperature diffraction patterns. (d) Temperature dependence of the pseudo-cubic lattice parameters, a_c and c_c; and the unit cell volume of the pseudo-cubic unit cell determined using neutron diffraction data. Error bars lie within the points.
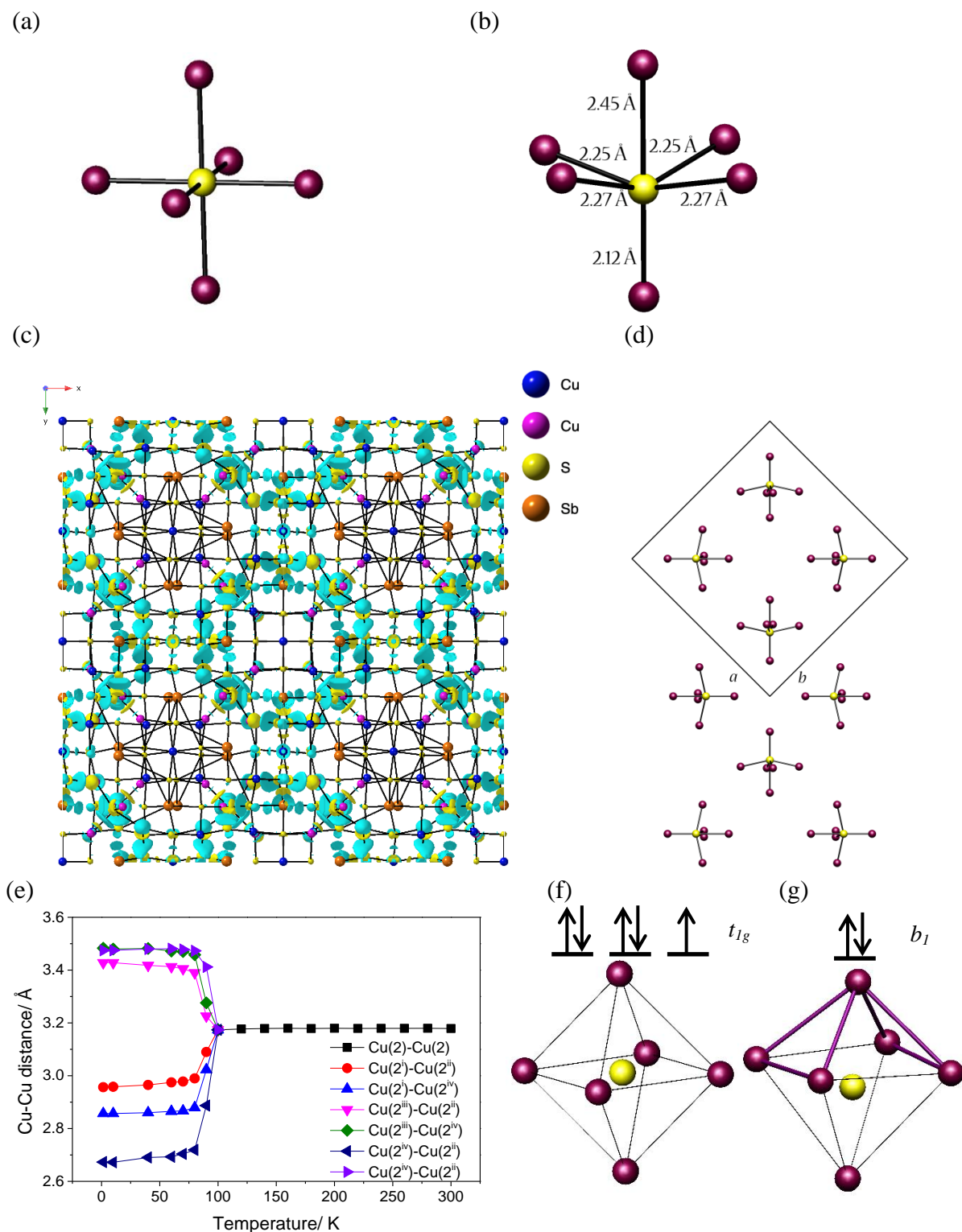
19

Figure 3. – (a) The SCu$_6$ octahedron in the cubic phase; all Cu-S distances are 2.25 Å. (b) The SCu$_6$ octahedron in the tetragonal phase, showing the Cu-S distances. (c) Difference between the ELF map of the cubic and tetragonal phases, showing marked changes around the SCu$_6$ octahedra only. Key: yellow indicates top 25% positive difference, blue corresponds to bottom 25% negative difference. (d) View of the tetragonal structure along [001] illustrating the alternation in displacement of S(2), with only SCu$_6$ octahedra shown. Unit cell also shown. (e) Temperature dependence of Cu-Cu distances between trigonal planar Cu(2) cations determined using neutron diffraction data. (f) SCu$_6$ octahedron in the high-temperature cubic phase, highlighting Cu-Cu distances shown in (e). The occupancy of the HOMO is shown. (g) SCu$_6$ octahedron in the low-temperature tetragonal phase, highlighting the distances shown in (e). The occupancy of the HOMO is shown. Key: Purple spheres, copper atoms; yellow spheres, sulfur atoms. Cu-Cu distances below 3 Å are shown as thick purple lines.
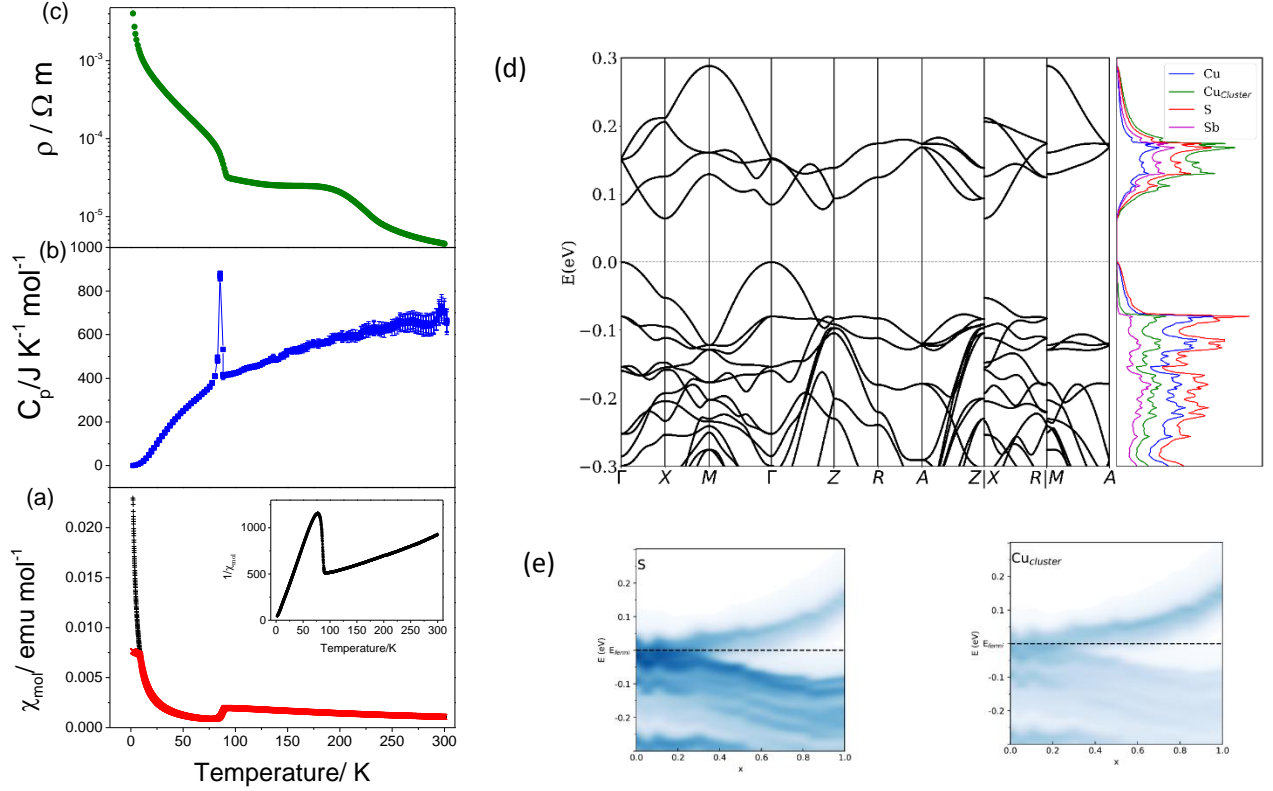
20

Figure 4. – (a) Temperature dependence of the magnetic susceptibility of $Cu_{12}Sb_4S_{13}$ under: Red –Field-Cooled conditions; Black – Zero-Field-Cooled conditions. Inset shows the reciprocal magnetic susceptibility. (b) Temperature dependence of the molar specific heat capacity for $Cu_{12}Sb_4S_{13}$. (c) Temperature dependence of the electrical resistivity for $Cu_{12}Sb_4S_{13}$. (d) Electronic band structure and partial density of states for tetragonal $Cu_{12}Sb_4S_{13}$ showing the band gap that opens. (e) Partial density of states for S and the Cu_5^{7+} cluster as a function of the distortion x (where x=0 corresponds to the cubic structure and x =1 to the tetragonal structure).
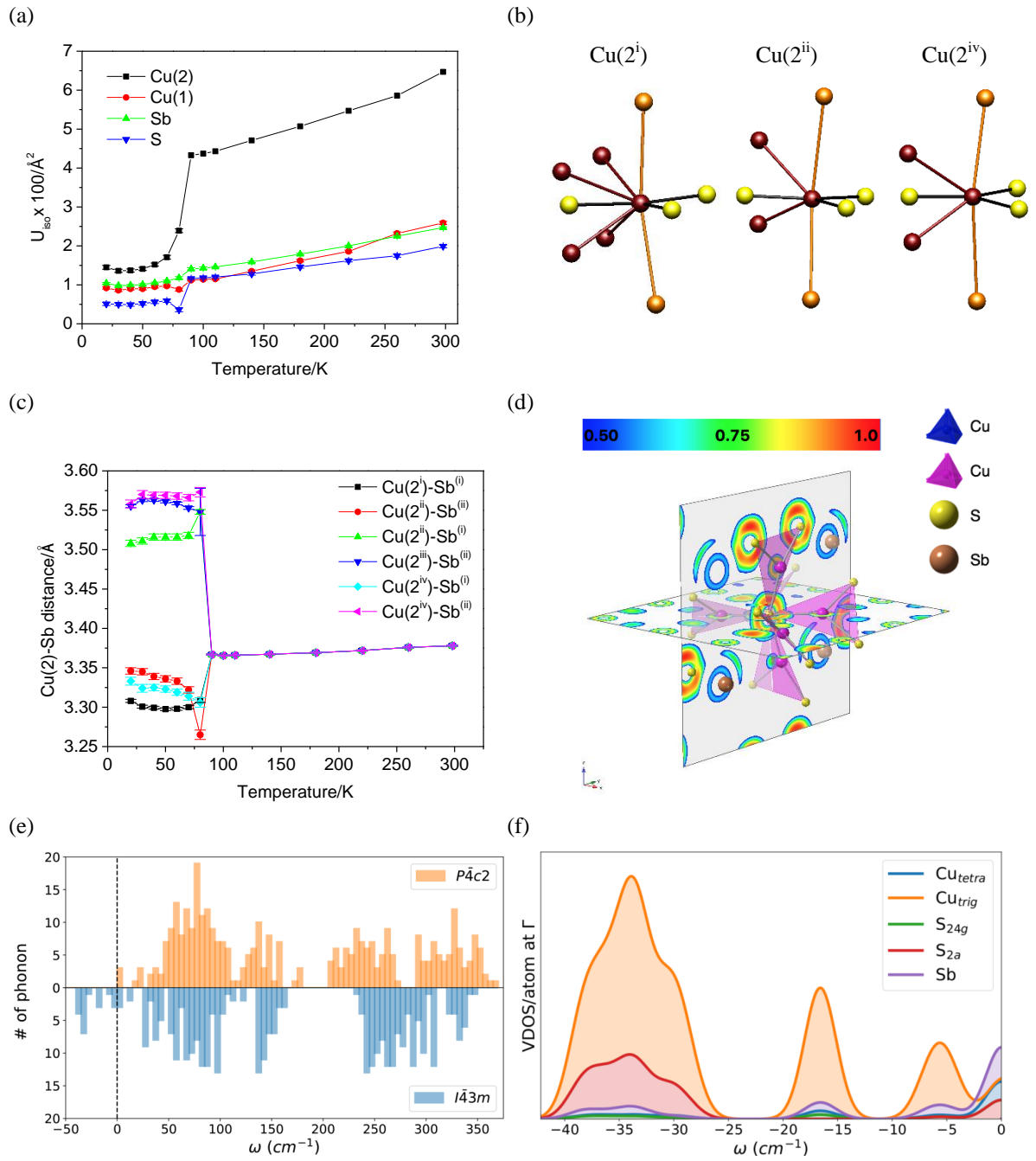
21

Figure 5. -(a) Atomic displacement parameters as a function of temperature, determined using synchrotron X-ray diffraction data. (b) Coordination environment of the trigonal-planar Cu(2) cations forming the pentamer in the tetragonal phase. Key: Purple spheres, copper atoms; yellow spheres, sulfur atoms; orange spheres, antimony atoms. (c) Cu(2)-Sb distances as a function of temperature (d) ELF map of the SCu_6 octahedron in the tetragonal phase, showing the Sb lone pairs. (e) Phonon spectrum for tetragonal and cubic tetrahedrite at the Γ point. (f) Vibrational density of states for the cubic phase at the Γ point projected on each element.

Table of Contents
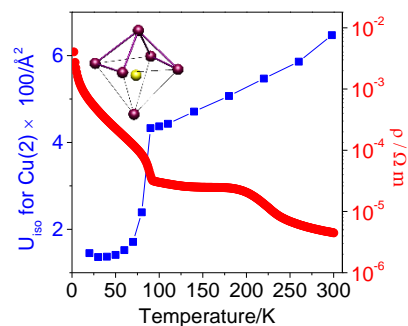
ToC keyword: thermoelectrics

Direct copper-copper interactions in tetrahedrite result in the formation of pentameric Cu_5^{7+} clusters below the metal-to-semiconductor transition. The enhancement of copper-copper interactions in these "molecular-like" clusters "locks" the trigonal-planar copper cations in place, suppressing the out-of-plane rattling vibrations to which low thermal conductivity is attributed.